scientific reports

Check for updates

OPEN

Effect of deposition rate on micromorphology analyses and optical parameters in amorphous carbon nickel thin films

Mostafa Khanmohammadi Padervand, Vali Dalouji✉ & Dariush Mehrparvar

In this work, the micromorphology of the Ni @ amorphous carbon films and their relationship to other optical properties using atomic force microscopic (AFM) imaging were examined. The surface topography of these Ni @ amorphous carbon sheets was reported using stereometric analysis and the SPIPTM 6.7.4 software in compliance with ISO 25178-2:2012 and ASME B46.1-2009. It is clear that the Ni @ amorphous carbon films deposited at 180 s had more the root mean square height (*Sq*) at around of 0.1475 mm and has the greatest value in comparison to other films. The Ni @ amorphous carbon films deposited at 600 s had a more regular surface because their the root mean square height (*Sq*) had minimum value of 0.1360 mm. The peak energy positions of optical density for the films deposited at 180 s which were the lowest value and about of 1.65 eV, could be due the quasi-metallic mode. The cut-off energy for the skin/shell depth parameters of the Ni @ amorphous carbon films were about 3.5 eV/ or 353 nm. The Ni @ amorphous carbon films deposited at 180 s had the lowest value of the electron - phonon interaction energy, (*Ee-p*). The small polaron model shown that as input photon energy was increased, the calculated AC conductivity by optical data for the Ni @ amorphous carbon films was decreased.

Keywords Atomic force microscopy (AFM) images, The micromorphology analyses, The Ni @ amorphous carbon films, Deposition time, Deposition rate, The absorption coefficient

The amorphous thin films, as composite configuration possessing have many interesting properties in nanotechnology, catalysts, optics, electronics, opt-electrical device, and surface morphology[1–3].

Among this wide range of amorphous materials that are made in the form of thin films, a group of them are completely transparent, which are used for purposes and applications that require the passage of photons with a high percentage, such as solar cells, while others are dark and opaque, which are used for applications opposite to those mentioned above, such as light-emitting diodes (LED). Such films, which can be made from transparent to dark films by changing the deposition time and also the deposition rate, are carbon/metal composite films that have many applications in the catalytic and optoelectronic industries and integrated circuits[4,5]. The amorphous carbon metals have a wide range of uses as coating materials in the mechanical, optical, electrical, and biological domains[6].

These light-emitting diodes materials films (LEDMF) work with different photon energy, especially based on nonlinear optical properties, which has attracted the attention of many researchers and published works for these field such as the composite amorphous thin films[7]. In addition to the use of this type of amorphous semiconductor thin films in the emission of photons of different wavelengths, their use can be used in the manufacture of information storage devices, the technology of quantum computer, optical switching, transmission of data processors after their processing, and also as optical waveguides[8,9]. Amorphous carbon matrices, which can be a very suitable host for keeping metal pollutants, especially transition metals, can be a small part of this type of new and practical composites[7,8].

Also, in addition to above applications, this type of amorphous semiconductor thin films can be applied as biotechnology, biochemical, biophysics and for specially only electronic devices, in dry medium and without hydrogen elements, and for optical devices, in dry medium and non-dry medium[8,9].

Because, these films acquire extraordinary properties compared to their single-phase counterparts, nanocomposites consisting of nanoparticles (NPs) or nanocrystals embedded in a matrix have been the subject of several studies[10,11].

Department of Physics, Faculty of Science, Malayer University, Malayer, Iran. ✉email: dalouji@yahoo.com

The inclusion of metal atoms may result in other interesting properties, such as a way to control tension and film adhesion[12].

In nanomaterials in the form of amorphous composite thin films by sputtering, two key elements are always effective in the role of the final fabricated films, which host the nanoparticles, both the type of nanoparticles injected into the matrix and the type of amorphous matrix that actually hosts the particles. Structural phase changes, both for metallic particles and for insulating particles, can strongly affect the physical properties of the final deposited films[13,14].

If under specific laboratory conditions the interaction effect between the matrix and metal particles is strong, in addition to the electrical and optical properties of the layers that are strongly affected, the mechanical properties and hardness of the deposited layers become very important in this situation. In this case, the layers can be used as good candidates for a variety of devices whose hardness is comparable to that of diamond[13–16]. The high level of resistance, durability, and immutability, as well as physical, thermal, and chemical balance, as well as photocatalytic applications and applications in different environmental times and places, have made the presence of metal particles in amorphous matrices as hosts, the cheapest and most accessible nanocomposites that have attracted the attention of many researchers[17,18]. In the past, we investigated many properties of this new compound, carbon films doped by metal particles were based on hydrogenated amorphous carbon films created by physical vapor deposition and chemical vapor deposition techniques. Conversely, less focus has been placed on the non-hydrogenated molecules. In this work, we tried to make non-hydrogenated composite films at ambient temperature. Since Ni, an element with a low affinity for carbon, forms a relatively sharp boundary between the metallic phase and the carbon matrix, Ni atoms were introduced to carbon sheets[19,20].

But in this new work, we intend using AFM obtained files data, to study some nonlinear topographical properties of these materials (for example; distribution of nanoparticles on films surface, the height distribution histograms and integration curve…) by using micro texture studies of these films using the SPIP™ 6.7.4 software, according to ISO 25178-2:2012, in room temperature, were calculated. Here, an explanation is necessary to mention that the above-mentioned software does not work offline and in a very limited way, and that only online. By providing the data file of images AFM images, they were possible, with great difficulty, to obtain the microanalysis graphs of the films' surface and all the data and results presented in Table 1. We then investigate some nonlinear optical loss and other optical parameters of the Ni @ amorphous carbon films deposited at different deposition times on glass substrates in room temperature. By obtaining some new optical parameters of these films and their relationship with their surface quality, let's implement a mathematical simulation model with these non-linear optical properties. The important aim of this paper, was also explanation of the relation between morphology micro strains parameters of the Ni @ amorphous carbon films deposited at 600 s on glass

The statistical parameters	Symbol	50 s	90 s	180 s	600 s
Amplitude parameters					
Arithmetic mean height	Sa (mm)	0.07677	0.09975	0.1021	0.09287
Root mean square height	Sq (mm)	0.1148	0.1433	0.1475	0.1360
Surface skewness	Ssk (–)	0.6513	0.4355	0.2272	0.6822
Surface kurtosis	Sku (–)	5.622	4.684	4.574	5.348
Maximum height	Sz (mm)	1.538	1.538	1.418	1.535
Maximum valley depth	Sv (mm)	0.7345	0.7363	0.7229	0.7338
Maximum peak height	Sp (mm)	0.8033	0.8014	0.6949	0.8015
Hybrid parameters					
Area root mean square slope	Sdq6	1.002	1.231	1.208	1.055
Surface area ratio	Sdr (%)	26.37	41.68	41.53	30.60
Reduced summit height	Spk (mm)	0.2254	0.2496	0.2419	0.2616
Core roughness depth	Sk (mm)	0.1367	0.1966	0.1985	0.1748
Reduced Valley depth	Svk (mm)	0.1507	0.1910	0.2157	0.1580
Spatial parameters					
Texture direction index	Stdi (–)	0.0931	0.07448	0.07448	0.07448
Dominant radial wavelength	Srw (mm)	48.218	21.668	37.708	14.505
Radial wave index	Srwi (–)	1.63	0.41	0.383	0.253
Functional Parameters (Volume)					
Material volume	Vm (mm^3/mm^2)	0.01026	0.01143	0.01137	0.01188
Void volume	Vv(mm^3/mm^2)	0.1519	0.1889	0.1893	0.1819
Peak material volume	Vmp(mm^3/mm^2)	0.01026	0.01143	0.01137	0.01188
Core material volume	Vmc(mm^3/mm^2)	0.07474	0.1015	0.1027	0.09443
Core void volume	Vvc(mm^3/mm^2)	0.1369	0.1699	0.1678	0.1658
Pit void volume	Vvv(mm^3/mm^2)	0.01502	0.01904	0.02151	0.01606

Table 1. The statistical parameters for the Ni @ amorphous carbon films at different deposition times 50, 90, 180, and 600 s according to ASMEB46.1–2009 and ISO 25178-2:2012.

substrates in room temperature with AC electrical which were measured using by optical absorption coefficients spectra.

Experimental details

The whole deposition process of different Ni @ amorphous carbon films on glass and quartz substrates at room temperature were shown conceptually Fig. 1 (a). Before these different Ni @ amorphous carbon layers were deposited, solid graphite targets (of high purity, 99.99%) were made using a rf magnetron VAS-sputtering system. The targets were 5 mm in thickness and 100 mm in diameter along with14 strips, or nickel pieces with a high purity of 99.99%, were then placed radially from the graphite target's center. They were 40 mm long and around 1 mm wide. The strips were positioned like matchsticks. The composite target (C/Ni), which was made up of a graphite base and nickel enhancements, was now positioned in its proper position within the vacuum chamber of the RF-magnetron sputtering system (VAS model). The composite target is consistently positioned in the cathode of the rf magnetron VAS-sputtering system until it is attacked by the positive plasma ionization of highly ionized argon gas with an energy of approximately 30 keV. The glass and quartz slides, which were the substrates used for the deposition processing, were decontaminated for 20 min using an ultrasonic device that contained distilled water and ethanol. Subsequently, they were desiccated using heated air flow. Before attaching the devices to the device receptacles, we employed specialized forceps to sanitize the side of the devices that had the material deposited on it. We deposited films on these substrates slides after preparing the substrates and installing them on specific holders in the device. A good and suitable vacuum (basic pressure in the range of 2×10^{-4} to 5×10^{-5} millibar) was then used to clean all contamination inside the device chamber. The plasma

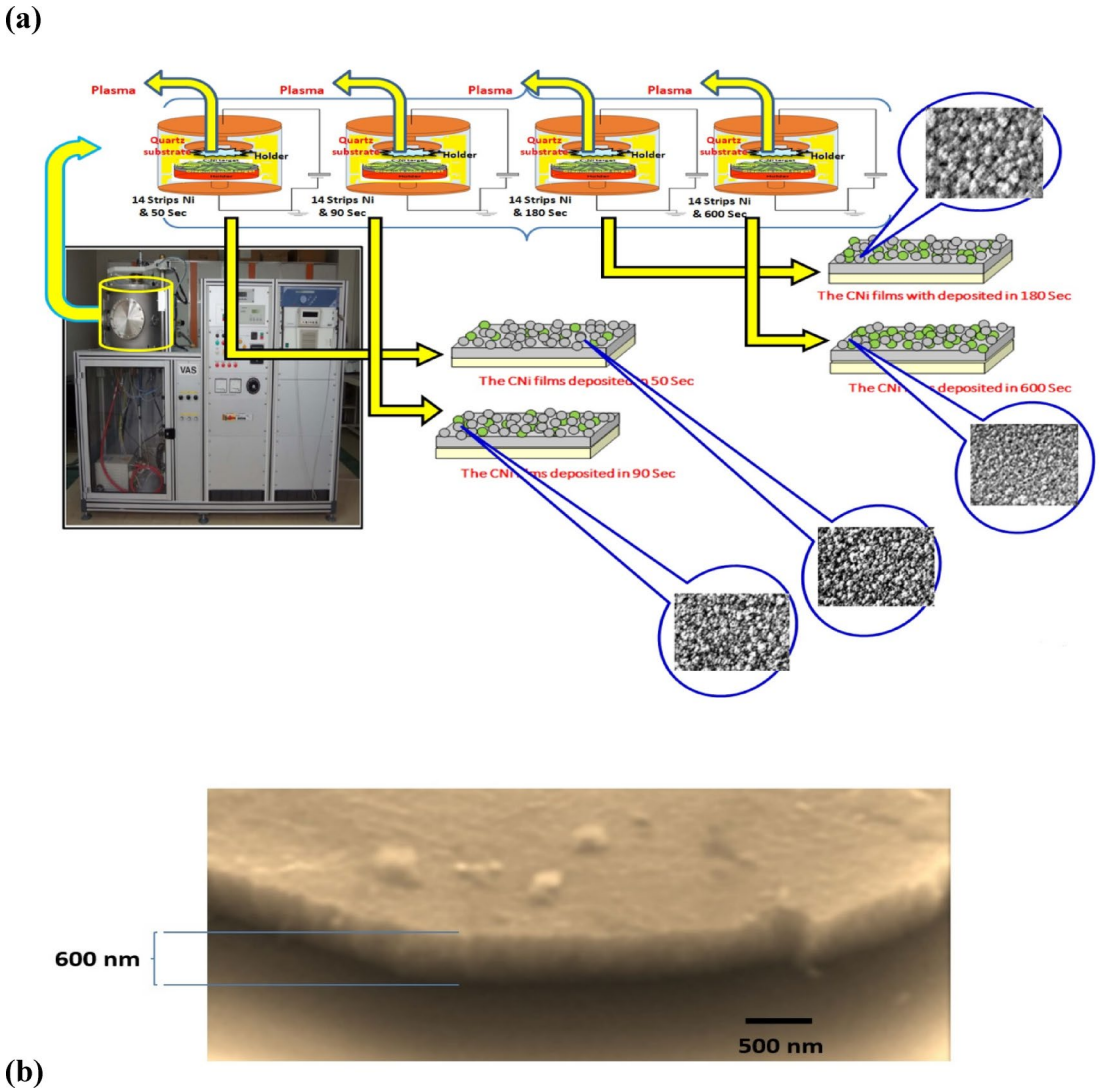

Fig. 1. (**a**) Schematic and real images for experimental details of the surface of the Ni @ amorphous carbon films deposited on glass substrates in room temperature, RF - magnetron sputtering device VAS, and images of films deposited at room temperature, (**b**) the cross section FESEM of the Ni @ amorphous carbon films deposited at 600 s.

necessary for deposition was created at a suitable working pressure of 2×10^{-2} to 2×10^{-3} millibar. The glass and quartz substrates were to have an RF power of approximately 400 ± 5 W. The thickness of these films deposited at all diverse deposition times could be measured using the Tencor Alpha Step 500 profiler method (Fig. 1 (b)). Subsequently, a variety of Ni @ amorphous carbon films were formed at room temperature with deposition rates and durations that varied (50, 90, 180, and 600 s). In order to conduct physical studies and analyze data, it was necessary to implement a variety of analyses that produced suitable results, which were frequently attained through iteration. In accordance with the objectives of this manuscript, we have performed optical and surface measurements on these diverse Ni @ amorphous carbon films. The transmission and absorption spectra of these films at each specific wavelength were measured using the Jasco V-630-Japan spectrometer model. In this work, using the transmission and absorption spectra, the absorption coefficients spectra were calculated from to study other optical parameters applied in this manuscript.

The optical measurements were performed at ambient temperature and within the 250–800 nm wavelength range. In addition, we applied atomic force microscopy (AFM) in noncontact mode on a specific surface area of $276 \times 276\ nm^2$ to assess the surface topography of these diverse Ni @ amorphous carbon films, as well as to ascertain the root mean square (RMS) roughness of the films and the lateral dimension of surface nanoparticles. To more accurately estimate the size of nanoparticles on the surfaces of these diverse Ni @ amorphous carbon films and to characterize the morphology, field emission scanning electronic microscopy (FESEM) images were also employed, however as typical.

Results and discussion

Figure 2 illustrate the integration curves derived from AFM images and the height distribution histograms for the Ni @ amorphous carbon films deposited at different deposition times. The height histogram is represented by the

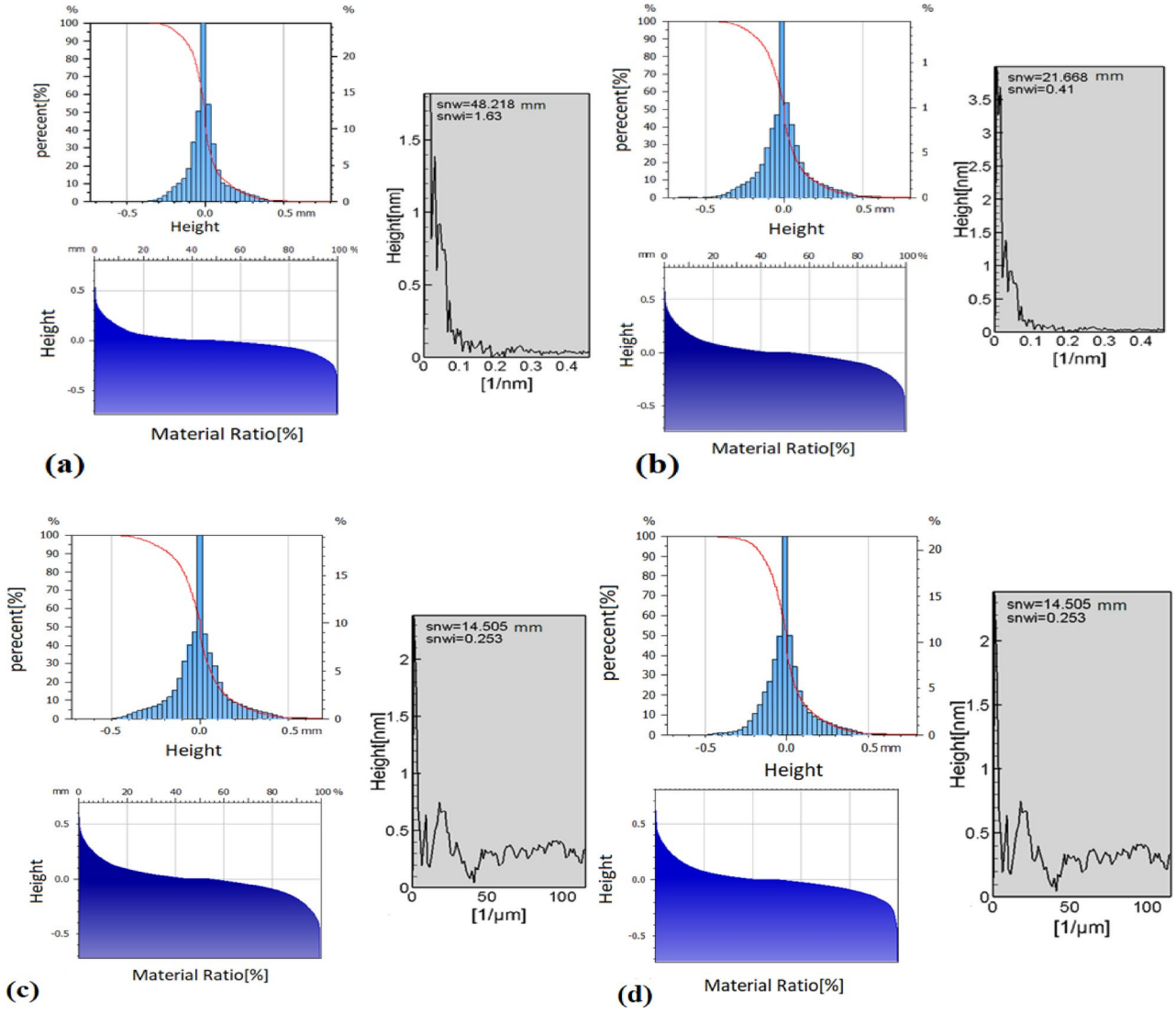

Fig. 2. The height distribution histograms, the integration curves and the Abbott-Firestone curves of the Ni @ amorphous carbon films at different deposition times (**a**) 50, (**b**) 90, (**c**) 180, and (**d**) 600 s.

number of fragments that appear on the surface in relation to a specific peak height, as well as the areal material curve that is positioned on the histogram. The height distribution histogram provides information regarding the surface's uniformity. The 90 s is characterized by the highest of the high range. The areal material curve, which contains parameter values of Sk, Svk, and Spk, is illustrated in the second diagram. The areal material curve is employed to calculate volume parameters, such as Vmp, Vmc, Vvc, and Vvv, using the third diagram. Figure 2also illustrates a graphical representation of the Abbott-Firestone curve for the Ni @ amorphous carbon films deposited at different deposition times that was computed for AFM images. The bearing ratio curve is a cumulative probability density function of the surface profile height that can be determined by integrating the profile trace in mathematical terms[21]. Films of nickel and carbon are associated with surface (Sa). Furthermore, the root mean heights (Sq) of the videos at 600 and 180 s were the largest and smallest, respectively. Furthermore, the surface that was more irregular (Sq = 0.1475 mm) was exposed after 180 s, while the surface that was more regular (Sq = 0.1360 mm) was unveiled after 600 s. The IAPSD function is the area of power spectral density (APSD) function that has been integrated for all angles of specified frequencies (inverse wavelength).

The main parameter from Table 1, are root mean square height, Sq, which actually reports the amount and measure of regularity and uniformity in the growth of nanoparticles accumulated on the surface of the deposited films. This symmetry and degree of regularity is relative to the vertical height. Of course, this parameter is the same as the root mean square of the roughness, which from a macroscopic point of view and software WSxM-2010 is called RMS, but from a microscopic point of view and software the SPIPTM 6.7.4 software in compliance with ISO 25178-2:2012 and ASME B46.1–2009, it is called Sq.

These parameters were obtained using atomic force microscopic (AFM) images in non-contact mode, of the as deposited 2D and 3D view of the films. According to the software WSxM-2010, which works using the data files of these images and outputs the results related to the surface morphology, the surface root means square roughness (RMS) values of for the films deposited on glass substrates in room temperature in deposition times of 50, 90, 180, and 600 s were obtained about 3, 4, 5 and 4 nm, respectively. The root means square height, Sq for the films deposited on glass substrates in room temperature in deposition times of 50, 90, 180, and 600 s were obtained about 0.1148, 0.1433, 0.1475 and 0.1360 mm, respectively.

Having more detailed information about the roughness of the films can be described the amount of scattering, transmission, reflection and absorption of incident photons on the deposition films to a large extent. Of course, this parameter can be considered a key factor in the study of the physical properties of the films if the other parameters of the films were constant. The key point that can be found in these physical effects is that the particles with a high rate of sputtering growth sit on the substrates, they do not find enough opportunity to find a point on the surface with the lowest potential energy level, as a result, the particle size increases and the surface roughness also was increased. The increasing and the topography curves of the surface of films will be asymmetric, on the contrary, when the particles with a low rate of sputtering growth sit on the substrates, they find a good opportunity to find a point on the surface with the lowest potential energy level, as a result, the size of the particles decreases and the surface roughness also was decreased and the surface topography curve will be symmetrical.

These physical interpretations strongly affect the values of the physical absorption coefficient of the films and then affect other physical properties as well.

The height distribution histogram provides information regarding the surface's uniformity for the films deposited on glass substrates in room temperature in deposition times of 50, 90, 180, and 600 s were in relation with parameters of reduced summit height, Spk (mm), core roughness depth Sk (mm), and reduced Valley depth Svk (mm), which actually reports the amount and measure of regularity and uniformity in the growth of nanoparticles deposited on the surface of the deposited films. This symmetry and degree of regularity is relative to the vertical height. Parameter of reduced summit height, Spk (mm), has the highest value of 0.2616 mm for the films deposited on glass substrates in room temperature in deposition times of 600 s, and parameters core roughness depth Sk (mm), and reduced valley depth Svk (mm), with values of 0.1748 mm and 0.1580 mm, respectively, have the lowest values for films deposited in 600 s compared to other films.

The maximum value in parameter reduced summit height, Spk (mm), means that the number of pixels in a scanned surface was related to films deposited in 600 s compared to other films. These pixels are actually the tips of the scanned nanoparticles in the swept cross-section. The larger the transverse size and, consequently, the larger the number of nanoparticles per unit area, the greater the numerical value of this parameter.

The minimum values for parameters core roughness depth Sk (mm), and reduced valley depth Svk (mm), for films deposited in 600 s compared to other films actually result in a uniform distribution of nanoparticles, with a smaller size than other deposited layers. In other words, if we take a macroscopic look at these three parameters, we can describe the distribution and abundance of nanoparticles for films deposited in 600 s compared to other films as Gaussian-shaped functions whose width at half maximum has the smallest value.

Figures 3 illustrate typical FESEM and AFM images of the Ni @ amorphous carbon films deposited at (a) 180 and (b) 600 s, respectively. The mean particle size estimated by AFM images for the films deposited at 50, 90, 180, and 600 s estimated to be in a bout of 9, 13, 20, and 16 nm, respectively. The mean particle size estimated by FESEM images for the films deposited at 50, 90, 180, and 600 s estimated to be in a bout of 16, 17, 80, and 19 nm, respectively.

The different deposition rate in these films causes making of different the sputtering mode which it strongly was affected on physical properties of films. As in manuscript were explained, because with increasing deposition time from 50 to 180 s deposition rate is increased and from 180 to 600 s it is decreased, therefore from 50 to 180 s the sputtering occurs in more metal content mode and from 180 to 600 s the sputtering occurs in more nonmetal content mode. Therefore, we expect that up to 180 s adsorptions atoms have not enough time to migrate to sites where the surface energy is low enough to be covered by the coming atom and as a result the films have large particle size. With increasing deposition time from 180 s to 600 s, adsorptions atoms have enough time

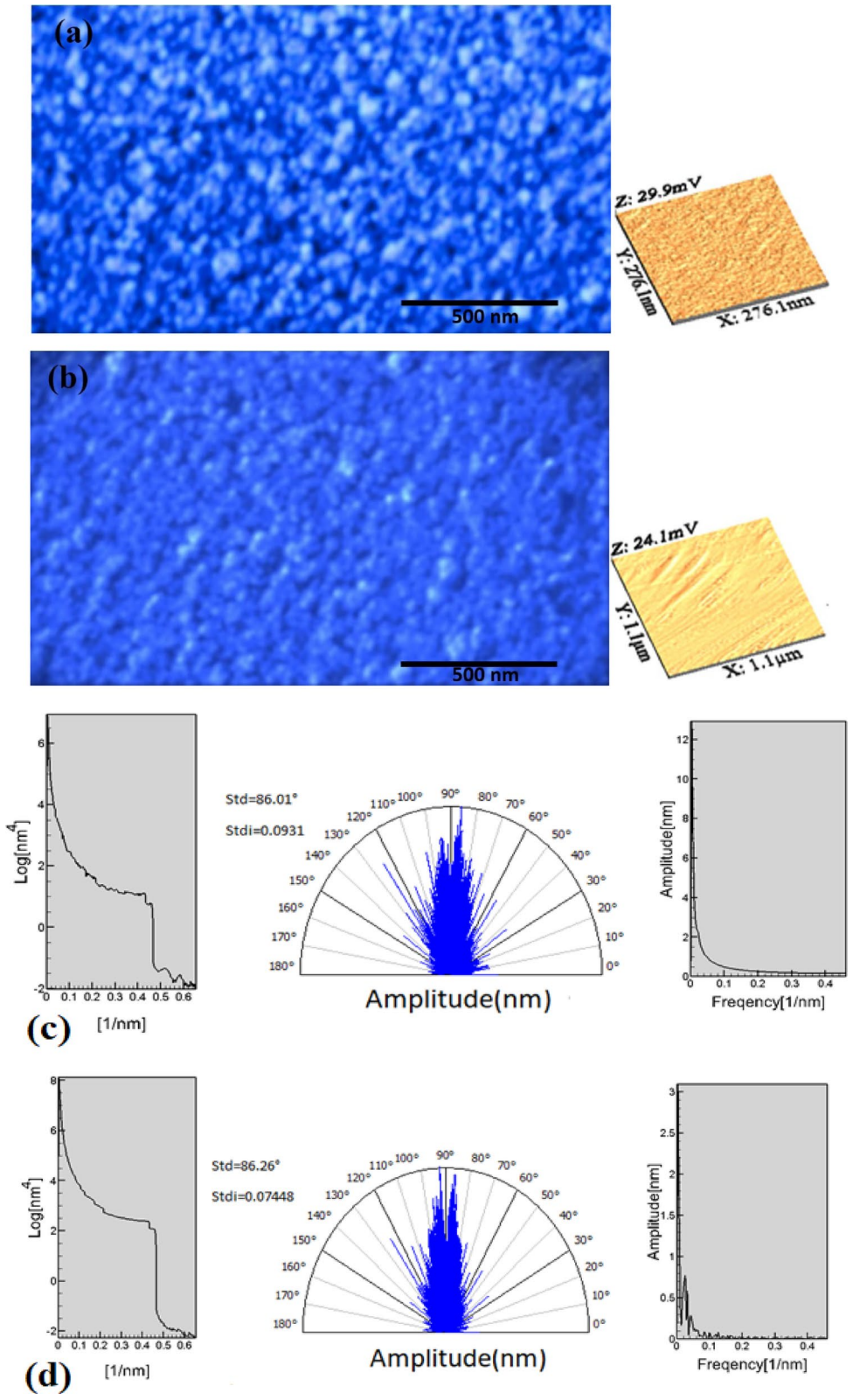

Fig. 3. The typical FESEM and AFM micrographs of the Ni @ amorphous carbon films at different deposition times (**a**) 180 and (**d**) 600 s, the average X-Fourier profile curves, the angular spectra and the isotropic area power spectral density (IAPSD) functions of the Ni @ amorphous carbon films at different deposition times (**c**) 50, (**d**) 90, (**e**) 180, and (**f**) 600 s.

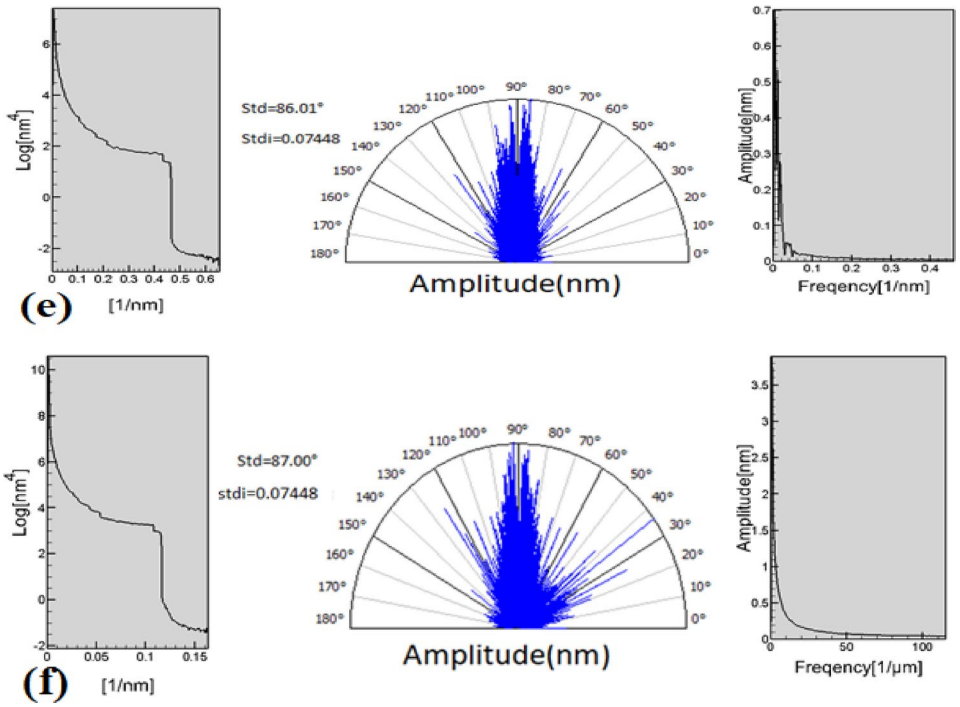

Figure 3. (continued)

to migrate to sites where the surface energy is low enough to be covered by the coming atom and as a result the films have small particle size. As a result, because nanoparticle sizes can be affected on physical properties of films, therefore micro surface and optical parameters of films strongly can be affected by different deposition times along with different deposition rates.

The EDAX spectrum for films deposited at different deposition times in line scan mode and one may observe the presence of characteristic peaks for C, Ni and Si. The Ni contents computed from the EDAX analysis were found to be 42, 48, 85 and 56 at% for films deposited at 50, 90, 180 and 600 s, respectively.

The surface topography was characterized using stereometric analysis with the SPIPTM 6.7.4 software, as per ISO 25178-2:2012 and ASME B46.1–2009[21–24]. The photos illustrate cementum, and Tables 1 and 2 summarize the stereometric results for the Ni @ amorphous carbon films deposited at different deposition times. All tissue shows a positive surface skewness (Ssk) (Ssk > 0), suggesting that cavities do not dominate the surface, with the highest amount occurring at 600 s (0.6822). The surface has high peaks and valleys because the surface kurtosis (Sku) of all samples is more than 4, with the lowest value happening in 180 s (4.574) and the greatest in 50 s (5.622). It is clear that the Sku decreased as the duration rose from 50 to 600 s. Figure 3 (c-f) depict the average X-Fourier profile curves of films across varied deposition times. Increasing the period from 50 to 600 s lowered the fractal dimension from Df = 2.01 ± 0.008 to *Df* = 2.01 ± 0.002. The sample with 50 s had the smoothest surface (Sa, Sq, Sz, Sv, and Sp had the lowest values), but the sample with 50 s had the most irregular topography (fractal dimension *D* = 2.01 ± 0.008), according to qualitative observations using statistical parameters of the *3-D* surface texture. Finally, Fig. 3 (c-f) show the angular and radial spectrums derived from AFM images. The angular spectrum was revealed the texture's direction. The principal texture directions were shown as peaks in this graph. Amplitude summation is another approach for determining relative amplitudes when *M* splits radial lines into equiangular segments. The radial spectrum is a scatter plot of the image's brightness amplitude as a function of wavelength. The core roughness height Sk, which is calculated by comparing the surface core's two extreme levels (maximal and minimum), is found to be highest for 180 s (0.1985 mm) and lowest for 50 s (0.1367 mm). The Svk

Samples	Deposition Time (s)	The wavelength of absorption edge (nm)	E_u (eV)	E_g (eV)	The constant (α_0) (nm)	Steepness parameter (σ)	(E_{e-p}) (eV)	RMS (nm)
#1	50	710.26	1.829	1.32	43.01	14.05E-3	**47.46**	4.20
#2	90	660.76	1.592	1.68	41.91	16.17E-3	41.24	3.30
#3	180	846.32	1.901	1.28	42.51	13.53E-3	49.27	3.40
#4	600	702.06	1.704	1.38	41.64	15.12E-3	44.01	2.12

Table 2. The values of (Eg), (EU), (σ), and (Ee-p) and RMS of for the Ni @ amorphous carbon films at different deposition times 50, 90, 180, and 600 s.

and Spk values reflect reduced dale height and decreased peak height, which were lowest at 50 s (Svk = 0.1527 mm) and 180 s (Spk = 0.2419 mm) and highest at 180 s (Svk = 0.2157 mm) and 600 s (Spk = 0.2616 mm).

The absorption coefficients of Ni @ amorphous carbon films can be calculated by UV-vis spectroscopy spectra, the following relation[21]

$$\alpha = \frac{1}{2}\ln\frac{\left(1 - R^2\right)}{2T} + \left(\frac{(1 - R)^4}{4T^2} + R^2\right)^{1/2} \quad (1)$$

where d were thicknesses of films, T were the spectral reflection of films, R were the spectral transmittance of films. By looking at the optical absorption coefficient spectra of the Ni @ amorphous carbon films, we find that for the entire wavelength range of photons incident on the surface of the layers (200 to 1000 nm), first the transmission spectra and then the reflection spectra were presented by the UV-vis spectroscopy device, and with the help of Eq. 1, the optical absorption coefficient spectra of the Ni @ amorphous carbon films were calculated according to Fig. 1. All these absorption coefficient spectra have maximum peaks in the range between 300 and 400 nm, which can of course be an estimate of the approximate values of the optical gap of the Ni @ amorphous carbon films. It is noteworthy that both the horizontal and vertical positions of these peaks do not have a linear relationship with the increase in the deposition time of the Ni @ amorphous carbon films at room temperature, and this is the most important result that we consider as a novelty and novelty of this important parameter, i.e. the deposition rate of the Ni @ amorphous carbon films at room temperature. As the deposition time of the Ni @ amorphous carbon films increases from 50 to 180 s at room temperature, the deposition rate of the layers increases from 0.8 to 1.7 nm/sec, and then as the deposition time of the Ni @ amorphous carbon films increases from 180 s to 600 s at room temperature, the deposition rate of the Ni @ amorphous carbon films decreases from 1.7 to 1 nm/sec. The maximum deposition rate in the films deposited at 180 s causes the particles that have landed on the substrates at room temperature to not have enough time before the arrival of the next particles to reach the lowest equilibrium potential energy level and lose all their velocity and kinetic energy and reach a stable equilibrium. Therefore, as the next and even next particles land, the height and size of these nanoparticles on the substrates increase, and the empty spaces between the formed nanoparticles also increase. This transverse and even vertical increase of nanoparticles in this case causes the volume of the grain boundaries to decrease, and then the grain boundaries scattering was decreased. This reduction in grain boundary scattering has a significant effect on the optical and electrical properties of the layers. However, with the vertical increase of nanoparticles in this case, it is expected that the root mean square roughness of the Ni @ amorphous carbon films will increase and, consequently, the scattering of incident photons on the surface of the layers will also increase. As can be seen in Fig. 4, after the Ni @ amorphous carbon films deposited in 50 s, the layers deposited in 180 s have the highest optical absorption coefficient due to the high deposition rate of 1.7 nm/sec. Then, for the Ni @ amorphous carbon films deposited in 600 s at room temperature, since the deposition rate decreases strongly and reaches approximately 1 nm/s, both the size of the nanoparticles and the root mean square roughness of the Ni @ amorphous carbon films decrease.

The sharp decrease in the accumulation rate in the Ni @ amorphous carbon films deposited in 600 s causes the particles landing on the substrates at room temperature to have enough time before the next particles arrive to reach the lowest equilibrium potential energy level and lose all their speed and kinetic energy and reach a stable equilibrium. Therefore, with the landing of the next and even next particles, the height and size of these nanoparticles on the substrates was decreased sharply, and as a result, the empty spaces between the nanoparticles formed on the surface of the Ni @ amorphous carbon films also decrease sharply. This sharp decrease in the transverse and even vertical size of the nanoparticles during this accumulation time of 600 s at room temperature causes the volume per unit area of the grain boundaries in the Ni @ amorphous carbon films was increased significantly, and then the grain boundaries scattering on the carriers passing through these

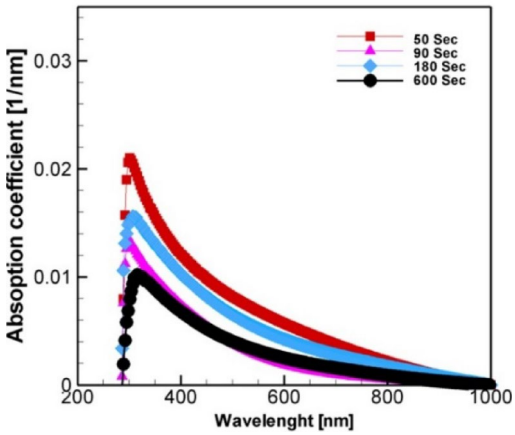

Fig. 4. The variations of absorption coefficient (α) of the Ni @ amorphous carbon films at different deposition times 50, 90, 180, and 600 s versus the incident photons wavelength (nm).

boundaries were significantly increased. This significant increase in the scattering of carriers by the boundaries has a great impact on the optical and electrical properties of the Ni @ amorphous carbon films.

As can be seen in Fig. 4, these the Ni @ amorphous carbon films deposited in 600 s have the lowest optical absorption coefficient due to the low deposition rate of 1 nm/s and the low root mean square roughness of the Ni @ amorphous carbon films. The smaller the size of the nanoparticles deposited on the layers and the more balanced their relative abundance and Gaussian distribution function (which is also true for the Ni @ amorphous carbon films deposited in 600 s), the smoother the Ni @ amorphous carbon films are and the more useful they are for many optoelectronic purposes. Figure 4 shows the changes in absorption coefficient (α) of the Ni @ amorphous carbon films versus the incident photons wavelength values for the films deposited at different deposition times of 50, 90, 180, and 600 s.

The optical density of the Ni @ amorphous carbon films can be obtained from the following Eqs[25,26]:

$$\mathrm{OD} = \alpha t \tag{2}$$

where t is the thin film thickness. Figure 5 (a) shows the changes in the optical density values for the deposited films at different deposition times of 50, 90, 180, and 600 s for different photon energies incident on the surface of the films.

As is clear from the figure, all graphs have maximum peaks that are in the photon energy range of 1.6 to 1.8 electron volts. With increasing photon energy up to these ranges, the optical density values for all films increase and then at energies higher than this range, the optical density values decrease. The location of these peaks varies for different films in terms of photon energy, and with changing photon energy, there are always shifts towards blue and red wavelengths. In other words, with changing photon energy, we see blueshift and redshift.

The change in the energy position of these peaks depends on the size of the nanoparticles on the films and also the thickness of the films. The energy position of this peak can be roughly considered as a measure of the optical gap energy (however approximately and not exactly) of the layers. The peak energy position in the films deposited at 180 s is the lowest and, as expected, these films are in the quasi-metallic mode and show a value of

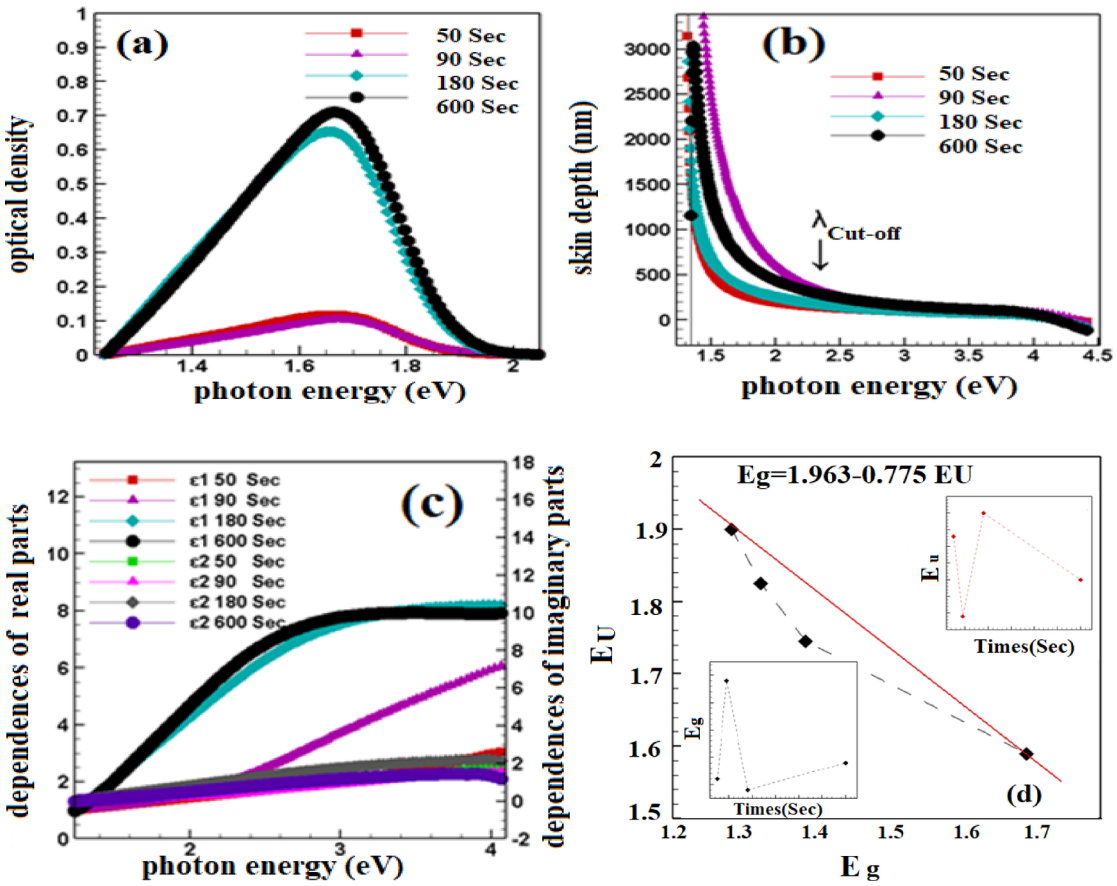

Fig. 5. (**a**) The relationship between photon energy (eV) and the optical density (OD) of films (**b**) the photon energy (eV) in relation to the skin/shell depth of films (**c**) The real and imaginary components of the complex dielectric are influenced by the energy photon (eV) of nanoparticles on the films surface by the axis for films. (**d**) the relationship between the energy band gap and the width of the Urbach tail with deposition times of Ni @ amorphous carbon films, as well as the variations of both the Eu and Eg and the dependency of doping on the optical energy gap and the band tail width.

about 1.65 eV. With a further increase in the deposition time to 600 s, the peak energy position shows a value of about 1.7 eV. The intensity of these peaks, i.e., their height (which are actually different numerical values without units), differs from each other because the growth rate and thickness of the layers are different. Due to the high thickness and high volume of metal nanoparticles inside the films deposited at 180 and 600 s, they have the highest intensity and height compared to the other the films and are numerically between 0.6 and 0.7.

Deposition periods dictate the height and placement of these peaks. It was also revealed that longer deposition periods increased the height of these peaks[27]. The "skin depth," or "δ," is the depth at which the current density is 1/e of the current density at the conductor's surface. It is a measurement of the skin effect. The natural logarithm is based on the mathematical constant "e" (about 2.718), which means that 1/e is approximately 37%. The skin depth is affected by the frequency of the current or signal as well as the resistivity of the material. The absorption coefficient (α) and skin depth (δ) are linked by the following simple relationship[28–30]:

$$\delta = 1/\alpha \tag{3}$$

Figure 5(b) shows the relation between skin depth and the films incident photon energy for the deposited films at different deposition times of 50, 90, 180, and 600 s. Following this photon energy value, the skin depth continuously decreased as photon energy rose, until reaching zero. The cut-off wavelength ($\lambda_{cut-off}$) and energy value (E-cut-off) refer to the matching wavelength and energy, respectively. Every film displays this tendency. The present film samples have a $\lambda_{cut-off}$ of 353 nm and an $E_{cut-off}$ of about 3.5 eV. After a significant distance, the absorption effect diminishes and the amplitude drops for photon wavelengths longer than the cut-off value ($\lambda_{cut-off}$ = 353 nm). Figure 5(c) depicts how the photon energy affects the real and imaginary components of ε_1 and ε_2 for films with different deposition periods. The variations of the optical dielectric constants (the real part and imaginary part of the optical dielectric constants ε_1 and ε_2) versus incident photon energy on a single plot can be resulted the optical band gap the Ni @ amorphous carbon films. In fact, the relationship between these two optical constants means that if we plot the changes in each of these optical constants in terms of the energy of the incident photons on the surface of the Ni @ amorphous carbon films on a common graph, the intersection of the graphs of these two constants with the line perpendicular to the x-axis, which is the energy axis, can be an estimate of the optical gap energy values of the Ni @ amorphous carbon films. Using this calculation method, the optical gap energy values for the Ni @ amorphous carbon films deposited on glass substrates in room temperature in deposition times of 50, 90, 180, and 600 s were calculated to be 1.32, 1.68, 1.28, and 1.38 eV, respectively. With increasing deposition time from 50 to 180 s, hence increasing the metallic mode, the energy optical band gap of thin films was decreased however with increasing deposition time from 180 to 600 s, hence increasing the nonmetallic mode (or decreasing the metallic mode), the energy optical band gap of thin films was increased. By observing the atomic force microscope images in the curved mode, this transition from non-metallic to quasi-metallic can be clearly confirmed in the Ni @ amorphous carbon films deposited at a deposition time of 180 s. This physical mode change, which is directly related to the increase in the Ni @ amorphous carbon films deposition rate in 180 s, not only affects the reduction in the optical gap energy of the Ni @ amorphous carbon films in 180 s, but also affects other optical properties and microparameters of the Ni @ amorphous carbon films surface.

The absorption coefficient of the Ni @ amorphous carbon films for incident photon energy less than optical gap depends on the photon energy exponentially[31,32]:

$$\alpha(h\nu) = \alpha_0 \exp(h\nu/E_U) \tag{4}$$

The transition between extended states in one band of absorption is known as E_U, or Urbach energy, and it is affected by temperature, induced disorder, average photon energies, strong ionic contacts, and lattice thermal vibrations[33]. Figure 5 (d) shows the relationship between the energy band gap and the width of the Urbach tail with deposition times of Ni @ amorphous carbon films.

The insets also illustrate how the ratio of deposition times in C-Ni films affects the optical band gap and the band tail energy. The observed changes in the optical band gap and the band tail energy were successfully examined using Mott and Davis's model[34,35]. The empirical formula for the linear fitting of the available film samples is as follows:

$$E_g = 1.963 - 0.775\ E_U \tag{5}$$

As well as, it can be seen from the above equation that the band gap energy value in the absence of tail (E_U = 0) is equal to 1.963eV[36,37]. The empirical formula for the linear fitting of these thin films were shown in Table 3.

Samples	Deposition time (s)	Line equation	E_0	E_d
#1	50	y = 0.55x + 16.23	3.24	3.15
#2	90	y = 0.63x + 15.70	3.02	3.03
#3	180	y = 0.53 x + 16.06	3.15	6.40
#4	600	y = 0.59 x + 15.63	3.28	9.32

Table 3. The obtained parameters values of the single-oscillator energy and dispersion energy parameter for the Ni @ amorphous carbon films at different deposition times 50, 90, 180, and 600 s.

The Urbach energy, E_U = kBT/σ(T), is a measure of the exponential tail's breadth in the absorption spectra at temperature *T*. Urbach[38] initially provided an equation that can be employed to visualize the absorption edge data and predict the amount of tailing to a first approximation.

$$\alpha = \alpha_0 \exp\left[\sigma\,(\mathrm{T})\;\;(\mathrm{E}-\mathrm{E}_0)\;/\mathrm{k_B T}\right] \tag{6}$$

where α is the absorption coefficient as a function of photon energy, E_0 and α_0 are the characteristic parameters of films, σ (T) is the steepness parameter, and k_B is Boltzmann constant. We rewrite Eq. (6) as follow

$$ln(\alpha) = ln(\alpha_0) + \left[\sigma\,(\mathrm{T})\;\;(\mathrm{E}\;/\;\mathrm{k_B T})\;\; - \sigma\,(\mathrm{T})\;\;(E_0/\mathrm{k_B T})\right] \tag{7}$$

The steepness parameter at each temperature was extracted by fitting the absorption data to equation $E_U = \mathrm{k_B T}/\sigma\,(\mathrm{T})$.

Where the steepness parameter is the Boltzmann constant and *T* is the absolute temperature. Moreover, the steepness parameter determined the strength of electron-phonon interaction (E_{e-p}) and both are related to each other following relationship[39]:

$$E_{e-p} = 2/3\sigma \tag{8}$$

The values of electron- phonon interaction and steepness parameter undergo changes over different deposition time values, as illustrated in Fig. 6 (a) and (b). The steepness parameter values increase as the temperature increases, while the electron-phonon interaction decreases. We investigated the relationships between the electronic and optical responses of films under temperature variations by determining the real component of optical conductivity (σ_{op}) from the imaginary dielectric constant (ε_2) and optical frequency (ω), where $\sigma_{op} = \varepsilon_2\omega/4\pi$. In the manner outlined below[40], the absorption coefficient can be employed to determine the optical conductivity σ_{opt} and the electrical conductivity σ_{elec}:

$$\sigma_{opt} = \varepsilon_2\omega/4\pi = \alpha nc/4\pi\varepsilon_2 = 2nk;\;\; k = \varepsilon_0\alpha\lambda; \qquad \omega = 2\alpha c/\lambda \tag{9}$$

$$\sigma_{elec} = (2\;L/\alpha)\sigma_{opt} \tag{10}$$

where the absorption coefficient is denoted by α and the light velocity is denoted by *c*. The changes in optical and electrical conductivity of Ni @ amorphous carbon films versus photon energy for films deposited at different deposition time 50, 90, 180, and 600 s versus photon energy were illustrated in Fig. 6(c) and (d). The electrical

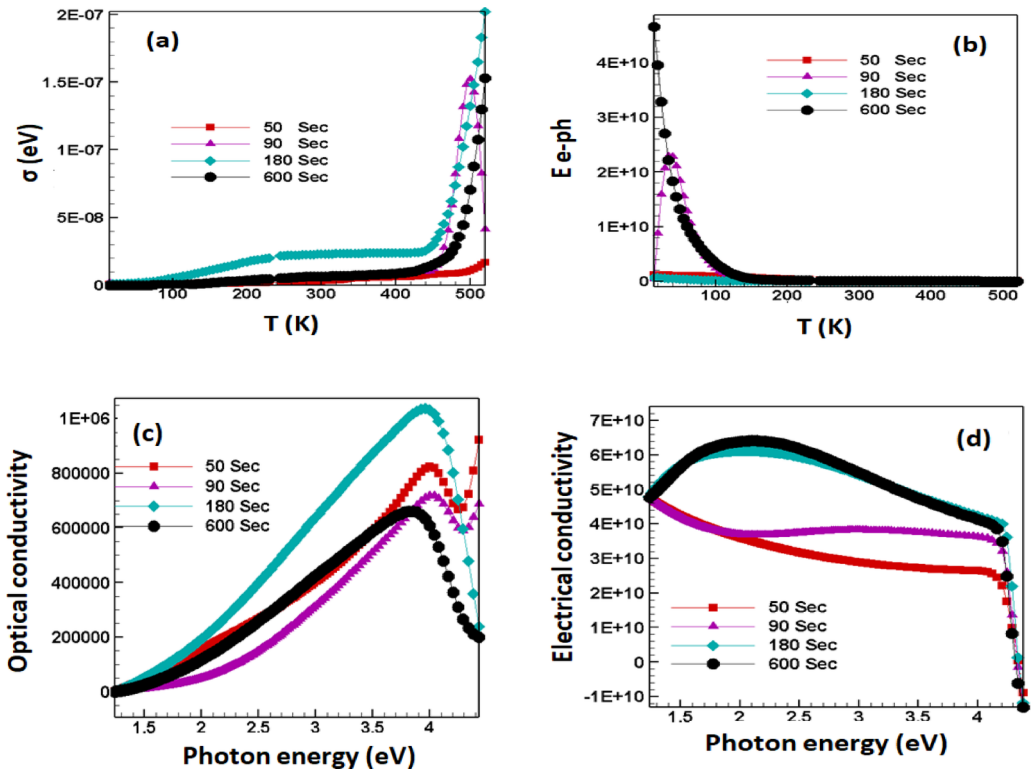

Fig. 6. Variations of both (**a**) the steepness parameter and (**b**) the electron phonon interactions of films versus temperature, (**c**) the variation of optical and (**d**) electrical conductivity of the Ni @ amorphous carbon films versus photon energy for films deposited at different deposition time 50, 90, 180, and 600 s.

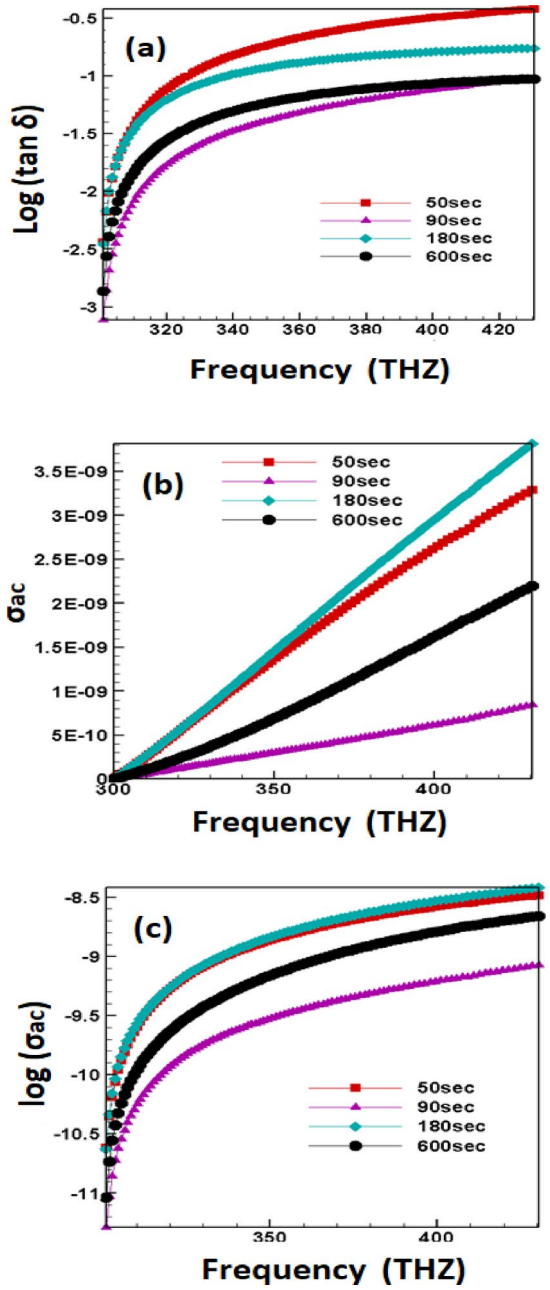

Fig. 7. (**a**) Variations of log (tan δ) versus photon frequency (**b**) frequency dependency *AC* conductivity and (**c**) the linear plots of log(σ_{ac}) versus photon frequency for the Ni @ amorphous carbon films versus photon energy for films deposited at different deposition time 50, 90, 180, and 600 s.

conductivities exhibit a similar behavior to the optical conductivity, which increases as the photon energy and annealing temperature of the films under investigation increase. The increase in optical conductivity at high photon energy may be attributed to the high absorbance of nanoparticles into films[41,42].

All samples demonstrate the same trend in the dielectric constant of the real and imaginary parts. The energy dissipation of the alternating external field is quantified and reported in terms of dielectric loss. The lagging of polarization in the application of the *AC* field, which is effectively caused by imperfections and dopants, results in dielectric loss. An additional explanation for the degradation of ε' and dielectric loss tan(δ) is a decrease in density that is a result of an increase in porosity (Fig. 7(a)). The graphs of *ac* conductivity for the Ni @ amorphous carbon films deposited at different deposition time 50, 90, 180, and 600 s versus photon frequency were presented in Fig. 7(b). The conductivity was calculated applying the relation (16)[43,44]:

$$\sigma_{\mathrm{ac}} = 2\pi f \varepsilon_{\mathrm{o}} \varepsilon' \tan\delta = 2\pi f \varepsilon_{\mathrm{o}} \varepsilon'' = \omega \varepsilon_{\mathrm{o}} \varepsilon'' \qquad \tan\delta = \varepsilon''/\varepsilon' , \qquad \omega = 2\pi/\mathrm{T} = 2\pi f \qquad (11)$$

where f is the frequency in Hz, ω is the angular frequency, εo is the permittivity of free space, and ε', ε'' are the real and imaginary components of the thin film's permittivity. Conductivity decreases as temperature rises. The $\log(\sigma_{ac})$ against photon frequency plots for the Ni @ amorphous carbon films deposited at different deposition time 50, 90, 180, and 600 s were used to estimate the polaron type of the hopping mechanism, as shown in Fig. 7(c). The alternating current conductivity increases in the large polaron model, while it decreases in the small polaron model as the frequency increases. The present investigation indicates that the AC conductivity exhibits a nearly linear relationship with increasing frequency, indicating that conduction hopping is accompanied by a minute polaron mechanism. At lower frequencies, grain borders are the primary factor influencing conductivity; however, grains have a more significant impact on conduction at higher frequencies[44,45].

Conclusion

In this paper, firstly the micro texture parameters of the surface of the Ni @ amorphous carbon films deposited on glass substrates in room temperature were obtained and investigated by by the SPIPTM 6.7.4 software in compliance with ISO 25178-2:2012 and ASME B46.1–2009 software.

Then, some optical parameters such as optical density, the skin/shell depth of films and electron-phonon interaction, were investigated.

Finally, a set of first-order linear mathematical equations extracted by different values of optical gap energy and Urbach disorder energy were investigated. Then, using these optical results, an estimate of the values of *ac* electric conductivity and their changes in terms of different values of incident photon frequencies on the films surface for the Ni @ amorphous carbon films were investigated. The key and important results for these analyses were presented below:

1) The Ni @ amorphous carbon films deposited at 600 s have maximum of the uniformity in nano particles distribution.
2) The Ni @ amorphous carbon films deposited at 180 s have maximum value of the nano particles mean height on the surface.
3) The Ni @ amorphous carbon films deposited at 50 s have maximum of irregular surface.
4) The Ni @ amorphous carbon films deposited at 180 s have maximum value of root mean square height, Sq, in a bout of 0.1475 mm.
5) The Ni @ amorphous carbon films deposited at 180 s have maximum value of core roughness depth, Sk, in a bout of 0.1985 mm.
6) The Ni @ amorphous carbon films deposited at 50 s have minimum value of core roughness depth, Sk, in a bout of 0.1367 mm.
7) The Ni @ amorphous carbon films deposited at 600 s have maximum number of Material volume, on their surface in a bout of 0.01188 mm^3/mm^2.

The Ni @ amorphous carbon films deposited at 600 s have minimum value of the optical loss. It was also found that, in high frequencies, the *ac* electric conductivity of the Ni @ amorphous carbon films deposited at 90 s has maximum values.

Data availability

The data that support the findings of this study are available from the corresponding author upon reasonable request.

Received: 13 January 2025; Accepted: 29 April 2025
Published online: 10 May 2025

References

1. Mott, N. F. & Davis, E. A, electronic processes in noncrystalline materials, 2nd, clarendon press- oxford, ISBN 978-0-19-964533-6 (pbk), p.(270–292).
2. Davis, E. A. Optical absorption, transport and photoconductivity in amorphous selenium. *J. Noncrystalline Solids*. **4**, i07–116. https://doi.org/10.1016/0022-3093(70)90026-8 (1970).
3. Tauc, J. & New York. Amorphous and Liquid Semiconductors, Plenum Press. London and. ISBN·13: 978-1-4615·8707·1, Chap. 4, page 174. (1974).
4. Talu, S. et al. Multifractal spectra of atomic force microscope images of cu/fe nanoparticles based films thickness. *J. Electroanal. Chem.* **749**, 31–41 (2015).
5. Ghodselahi, T., Vesaghi, M. A. & Shafiekhani, A. Study of surface plasm on resonance of Cu@Cu2Ocore–shell nano particles by Mie theory. *J. Phys. D: Appl. Phys.* **42**, 015308 (2009).
6. Endrino, J. L. et al. Structure and properties of silver-containing a-C(H) films deposited by plasma immersion ion implantation. *Surf. Coat. Tech.* **202**, 3675–3682 (2008).
7. Chang, Y. Y., Wang, D. Y. & Wu, W. T. Catalysis effect of metal doping on wear properties of diamond-like carbon films deposited by a cathodic-arc activated deposition process. *Thin Solid Films* ; 420. (2002).
8. Ghodselahi, T., Vesaghi, M. A. & Shafiekhani, A. Metal–nonmetaltransition in the copper–carbon nanocomposite films. *Phys. B.* **405**, 3949–3951 (2010).
9. El-Nahass, M. M., Sallam, M. M., Samy Rahman, A. & Ibrahim, E. M. Optical, electrical conduction, and dielectric properties of TlGaSe2 layered single crystal. *Solid State Sci.* **8**, 488–499. https://doi.org/10.1016/j.solidstatesciences.2005.10.020 (2006).
10. Dalouji, V., Elahi, S. M. & Valedbagi, S. Multiphonon hopping conduction in carbon–nickel composite films at different deposition time. *Rare Met.* **37**, 143–147 (2018).
11. Talu, S. et al. *Electron. Mater. Lett.* ; **12**: 580–588. (2016).
12. Talu, S. et al. *Superlatt Microstruct.* ; **93**: 109–121. (2016).
13. Talu, S. et al. Surface micromorphology and fractal geometry of Co/CP/X (X = Cu, Ti, SM and Ni) nanoflake electrocatalysts. *RSC Adv.* **6**, 27228–27234 (2016).

14. Mahdavi, S., Amini, N., Merrikhpour, H. & Akhzari, D. Characterization of bare and modified nano-zirconium oxide (ZrO_2) and their applications as adsorbents for the removal of bivalent heavy metals. *Korean J. Chem. Eng.* **34**, 234–244 (2017).
15. Dalouji, V. & Asareh, N. Nonmetal–metal transition in carbon films embedded by nickel nanoparticles: absorption coefficients studies and Wemple–Didomenico dispersion parameters. *Opt. Quant. Electron.* **49**, 262 (2017).
16. Laidani, N., Calliari, L., Speranza, G., Micheli, V. & Galvaneto, E. Mechanical and structural properties of Ni-C films obtained by RF sputtering. *Surf. Coat. Technol.* **100** (101), 116–124 (1998).
17. Hauert, R. A review of modified DLC coatings for biological applications diamonds relat. *Mater* **12** (3–7), 583–589 (2003).
18. Narayan, R. J. Pulsed laser deposition of functionally gradient diamondlike carbon–metal nanocomposites. *Diamonds Relat. Mater.* **14**, 8: 1319–1330 (2005).
19. Dalouji, V. & Elahi, S. M. Study of structural, electrical and magnetic properties of RF-Magnetron sputtered Carbon–Nickel composite films at different deposition rate. *J. Fusion Energ.* **34**, 646–652 (2015).
20. Dalouji, V. Effect of deposition time on surface plasmon resonance and Maxwell-Garnett absorption in RF-magnetron sputtered carbon-nickel films. *Mater. Science-Poland*. **34** (2), 337–343 (2016).
21. Kovacs, G. J. et al. Structure and mechanical properties of carbon–nickel and CN_x–nickel nanocomposite films. *Surf. Coat. Technol.* ; 180–181, 331–334. (2004).
22. Ahmed, M., Nawar, A. R., Wassel, Shehab, E., Ali, Ahmed, M. & El-Mahalawy Realization temperature roles of in-situ ZnSe films growth toward efficient photodetection performance. *Surf. Interfaces*. **42**, 103415. https://doi.org/10.1016/j.surfin.2023.103415 (2023).
23. http://www.iso.org, accessed on: 2018.10.01.
24. https://www.asme.org, accessed on: 2018.10.01.
25. Rahimi, N. & Dalouji, V. The free carrier's loss, free carriers susceptibility, and optical VEL and SEL functions in ZnO films doped by Cu, al, and Cu-Al composite nanoparticles. *Indian J. Phys.* (2021).
26. Dalouji, V., Goudarzi, S. & Solaymani, S. (25), The optical density and topography characterizations of MWCNTs on Ni-Cu/a-C: H substrates with different copper percentage. Microscopy Research and Technique. (2020).
27. Ahmed Saeed, H. & Akl, A. A. Influence of composition on optical and dispersion parameters of thermally evaporated non-crystalline Cd50S50 – xSex thin films. *J. Alloys Compd.* **648**, 280–290 (2015).
28. Eloy, J. F. National School of Physics, Power Lasers, Grenoble, France. (1984).
29. Joydeep, D. et al. P. Growth of hierarchical strontium incorporated cadmium sulphide for possible application in optical and electronic devices. *J. Mater. Sci.: Mater. Electron.* **28** (2), 2049–2061 (2017).
30. Abbasi, P. & Dalouji, V. Influence of annealing processing on dissipation electrical energy, volume, and surface energy loss functions of CZO films. *Indian J. Phys.* ; 1–10. (2020).
31. Urbach, F. The long-wavelength edge of photographic sensitivity and of the electronic absorption of solids. *Phys. Rev.* **92**, 51324 (1953).
32. Tauc, J., Abraham, L., Pajasorv, R., Grigorovici & Vancu, A. Proc. Internat. Conf. Physics of Noncrystalline Solids, Delft 1964 North Holland Publ. Comp. (p. 606). (1965).
33. Sakr, G. B., Yahia, I. S., Fadel, M., Fouad, S. S. & Romčević, N. Optical spectroscopy, optical conductivity, dielectric properties and new methods for determining the gap States of cuse thin films. *J. Alloys Compd.* **507** (2), 557–562 (2010).
34. Mott, N. F. & Edward, A. *D. Electronic Processes in non-crystalline Materials* (Oxford University Press, 2012).
35. Abdel-Latif, A., Y, MahfozKotb, H., Hafiz, M. M. & Dabban, M. A. Influence of heat treatment on the structural, optical and electrical properties of Cd20Sn10Se70 thin films. *Mater. Sci. Semiconduct. Process.* **30**, 502–512 (2015).
36. Shadia Jamil, I. & Ahmad-Bitar, R. N. A study of the optical bandgap energy and Urbach tail of spray-deposited cds: in thin films. *J. Mater. Res. Technol.* **2**, 3: 221–227 (2013).
37. Ebrahimi, S., Benyamin, Y. & Naderi, N. Effect of the sulfur concentration on the optical band gap energy and Urbach tail of spray-deposited ZnS films. *Adv. Ceram. Progress*. **3** (4), 6–12 (2017).
38. Riungu, G. G., Mugo, S., Ngaruiya, V., Fouad, V. & Romčević, S. S. Optical band energy, Urbach energy and associated band Tails of nano crystalline TiO_2 films at different annealing rates. *Am. J. Nanosciences*. **7** (1), 28–34 (2021).
39. Vettumperumal, R., Kalyanaraman, S., Santoshkumar, B. & Thangavel, R. Estimation of Electron-Phonon coupling and Urbach energy in Group-I elements doped ZnO nanoparticles and thin films by sol-gel method. *Mater. Res. Bull.* **77**, 101–110 (2016).
40. Pankove, J. I. *Optical Processes in Semiconductors* (Courier Corporation, 1975).
41. Yakuphanoglu, F., Cukurovali, A. & Yilmaz, I. *Opt. Mater.* ; **27**:1363. (2005).
42. Rahimi, N., Dalouji, V. & Rezaee, S. Effect of annealing processing on morphology, spectroscopy studies, Urbach disordering energy, and WDD dispersion parameters in Cu-Al doped zinc oxide films. *J. Dispers. Sci. Technol.* **43** (7), 990–999 (2022).
43. Goudarzi, S., Dalouji, V. & Solaymani, S. The relation between the average diameter of CNTs on Ni-Cu @ a-C:H catalyst with the optical absorption edge and the optical dispersion parameters. *J. Microscopy* (2020).
44. Alia, I. et al. Effect of Tb-Mn substitution on DC and AC conductivity of Y-type hexagonal ferrite. *Alloys Compd.* **579**, 576–582 (2013).
45. Gul, I. H., Ahmed, W. & Maqsood, A. Electrical and magnetic characterization of nano crystalline Ni-Zn ferrite synthesis by co-precipitation route. *Magn. Magn. Mater.* **320**, 270–275 (2008).

Author contributions

"V. Dalouji wrote the main manuscript text and done some physical analysis's and M. Khanmohammadi prepared figures obtained from software data and D. Mehrparvar help us in answering to referees comments in revising manuscript. All authors reviewed the manuscript."

Declarations

Competing interests

The authors declare no competing interests.

Ethical approval

This is an original article. Of course, some of the other properties of this material have been reported in other articles, but the analyzes reported in this article have not been repeated anywhere.

Additional information

Correspondence and requests for materials should be addressed to V.D.

Reprints and permissions information is available at www.nature.com/reprints.

Publisher's note Springer Nature remains neutral with regard to jurisdictional claims in published maps and institutional affiliations.

Open Access This article is licensed under a Creative Commons Attribution-NonCommercial-NoDerivatives 4.0 International License, which permits any non-commercial use, sharing, distribution and reproduction in any medium or format, as long as you give appropriate credit to the original author(s) and the source, provide a link to the Creative Commons licence, and indicate if you modified the licensed material. You do not have permission under this licence to share adapted material derived from this article or parts of it. The images or other third party material in this article are included in the article's Creative Commons licence, unless indicated otherwise in a credit line to the material. If material is not included in the article's Creative Commons licence and your intended use is not permitted by statutory regulation or exceeds the permitted use, you will need to obtain permission directly from the copyright holder. To view a copy of this licence, visit http://creativecommons.org/licenses/by-nc-nd/4.0/.

© The Author(s) 2025